**IEEE Robotics and Automation Letters (RA-L) paper, presented at ICRA 2026, Vienna, Austria. Cite as RA-L paper.**

# In-Orbit Space Structure Inspection Trajectory Generation

Brandon Apodaca[1], Thor Helgeson[1], Ella Atkins[2], and Leia Stirling[3]

***Abstract*—Exterior International Space Station (ISS) visual inspection currently requires astronaut extravehicular activity (EVA), a safety risk. Free-flying space robots can perform visual inspection but risk station collision and high astronaut overhead for teleoperation. Existing inspection planners do not effectively co-optimize inspection coverage and energy consumption with consideration of both orbital dynamics and human supervisor situation awareness. This paper presents an inspection trajectory generation pipeline [1] that integrates orbital dynamics with robot coverage path planning methods to ensure collision avoidance and investigate situation awareness. Inspection trajectories meet thrust and space robot dynamics constraints while achieving 98% coverage with 17 grams of fuel on a space station model scaled to the ISS. Pareto front analysis balances fuel consumption with coverage directly. Presented solutions show that paths vary as a function of coverage versus energy prioritization. Methods in this paper contribute towards reducing risk posed to astronaut safety during space station operation and maintenance by providing trajectory generation algorithms towards external semi-autonomous in-orbit inspection of complex space structures.**

***Index Terms*—Space Robotics and Automation, Motion and Path Planning**

## I. Introduction

MAINTENANCE of complex structures in space requires inspection for anomaly detection (e.g., micrometeoroid and orbital debris impact, delamination). Current means for inspecting complex space-bound structures rely on astronaut extravehicular activity (EVA) to inspect areas in the blind spots of external cameras and outward facing windows [1]. A free-flying inspection robot can alleviate risk to astronauts, allowing them to indirectly inspect the station exterior via relayed sensor information from the inspection robot. Hardware capabilities for compact free-flying robotic inspection include AERCam [2] and Seeker [3]. However, existing trajectory planners for in-orbit external space station inspection do not directly optimize inspection quality, and inspection trajectory generators that directly optimize inspection quality do not incorporate orbital dynamics. Additionally, in-orbit inspection systems do not offer constraints that support a human supervisor's situation awareness, the supervisor's state of knowledge pertaining to the inspection environment [4]. This paper proposes a pipeline for a human-supervised semi-autonomous free-flying inspection robot that adapts viewpoint planning algorithms from the robotics literature, leverages orbital trajectory optimization techniques from space literature, and innovates a constraint that supports studying human situation awareness.

Current on-orbit structural inspection path planners do not optimize camera viewpoints that maximize information gain and minimize viewpoint traversal cost. On-orbit inspection path planning yields full coverage paths but constrains paths to an Archimedes spiral without considering energy use [5] or inspection quality [6]. On-orbit receding-horizon inspection trajectory planning [7] optimizes sun angle and orbit kinematics but converges towards locally optimal solutions less fuel efficient than global solutions. Optimal inspection trajectory planning generates fuel optimal paths but requires manually placed waypoints [3], [8], [9] or reference trajectories [10] that may not maximize coverage or minimize fuel use. In-orbit trajectory optimization techniques may formulate suboptimal coverage constraints and objectives for complex structures.

Terrestrial trajectory planners optimize inspection quality but do not consider orbital dynamics when minimizing traversal cost. Terrestrial inspection techniques decouple inspection planning into coverage maximization and traversal cost minimization problems and leverage camera optics, set theory supported viewpoint planning, and traveling salesman problem (TSP) methodology [11]–[14]. While algorithms like the TSP have been formulated for in-orbit context, they do not consider proximity operation viewpoint traversal scenarios [15], [16]. However, terrestrial inspection planners minimize path length or other terrestrial dynamics to minimize traversal cost, not frictionless in-orbit kinematics. Inspection path planners use Pareto fronts to allow a user to select solutions that balance competing coverage and traversal cost objectives from genetic algorithm solutions [17], [18]. However, they do not consider orbital dynamics and kinematics or leverage viewpoint planning methodology supported by set theory.

In-orbit and terrestrial inspection path planning methods do not include constraints or objectives that modulate situation awareness support that can improve damage detection by human supervisors. Heavy cognitive workload is associated with more frequent human errors and situation awareness support decreases cognitive workload [4], [19], [20]. View-

Received: Feb., 3, 2025; Revised May, 5, 2025; Accepted June, 8, 2025.

This paper was recommended for publication by Editor Ki-Uk Kyung upon evaluation of the Associate Editor and Reviewers' comments. This research was supported by the National Aeronautics and Space Administration (NASA) Human Research Program Award 80NSSC20K0409.

[1]Robotics Department at the University of Michigan, Ann Arbor, Michigan bapodaca@umich.edu; thelg@umich.edu

[2]Kevin T. Crofton Department of Aerospace and Ocean Engineering at Virginia Polytechnic Institute and State University College of Engineering, Blacksburg, Virginia, United States ematkins@vt.edu

[3]Industrial & Operations Engineering and Robotics Departments at the University of Michigan College of Engineering, Ann Arbor, Michigan, United States leias@umich.edu

Digital Object Identifier (DOI): see top of this page.

[1]Code accessible at https://github.com/bapodacaumich/ccpp_ral.git

**IEEE Robotics and Automation Letters (RA-L) paper, presented at ICRA 2026, Vienna, Austria. Cite as RA-L paper.**

point planning algorithm viewpoint generation distance (VGD, viewpoint to target proximity) is either user defined or computed from camera focal length [21]. However, no approaches consider the influence of VGD on supervisor perception of environmental elements (level 1 situation awareness) [4]. Typical inspection planners first separate the inspection target into sequential subproblems to simplify the approach [22]–[24]. Communication of subproblems and their sequence to a human supervisor influences supervisor situation comprehension (level 2 situation awareness) and projection of future environment status (level 3 situation awareness) [4] through improved autonomy intent transparency [25]. Although potential situation awareness modulation factors are available, their implementation is not structured to study their influence.

Inspection planning, orbital trajectory generation, and situation awareness support techniques do not provide an orbital supervised inspection generation pipeline that supports situation awareness modulation. This paper presents a trajectory generation pipeline that fills three gaps: (1) Integrates orbital dynamics and kinematics into optimization, (2) Leverages viewpoint planning, TSP methodology, and Pareto front information gain and fuel consumption co-optimization, and (3) Modulates VGD, which may affect level 1 situation awareness, and *local* constraint that may influence levels 2 and 3 situation awareness in human supervisors. Contributions include an extension of the TSP to include prior node traversal cost dependence, an inspection problem segmentation (*local*) constraint, decoupled viewpoint planning and trajectory generation pipeline for orbital inspection, and a coverage motivated waypoint proximity penalty. Results present a trade space analysis, contrasting with traditional impulsive maneuvering strategies.

## II. Methodology

In-orbit inspection trajectories require collision and robot kinodynamic constraint satisfaction, fuel consumption minimization, and information gain maximization. Unified approaches optimize information gain and fuel cost simultaneously but are computationally complex [26] or lack global optimality [27]. Decoupled planners optimize information gain and traversal cost sequentially leading to faster solution discovery and rarer local optima convergence than unified planners [11], [14]. This paper adapts the decoupled approach by incorporating situation awareness modulation factors, space robot dynamics, and waypoint proximity penalties.

Our approach (Figure 1) has three steps: (1) Generate viewpoints that maximize coverage (Section II-A), (2) Order maximal coverage viewpoints to minimize the heuristic fuel cost (Section II-B), and (3) Guide optimal-control-based trajectory generation with the ordered set of viewpoints (Section II-C). In viewpoint planning and ordering, an optional *local* constraint restricts trajectory subpaths to inspect different modules (Figure 2) to study their influence on situation awareness, where information gain (coverage quality, see Section II-A3) is maximized with respect to the corresponding module before continuing to the next subpath associated with another module. Fuel cost is still minimized with respect to overall path.

### A. Viewpoint Planning

A minimal viewpoint set is selected to maximize observation quality and quantity. Viewpoint planners rely on mesh primitives (vertices or faces), sampling, or both to maximize viewpoint information gain [21], [23], [27]. Set cover theory provides optimality guarantees for greedy information gain maximization [28], [29], [30]. This paper's approach processes the station mesh for viewpoint generation, generates viewpoints, then greedily builds a minimal coverage viewpoint set.

*1) Model Triangulation:* Dual contouring [31] modifies existing meshes for viewpoint generation. Parameters are adjusted so mesh face edges are approximately $0.5$m in length, yielding 1206 faces. This scale yields reasonable computation times for inspection trajectory generation. A face is covered when all vertices are visible from a single camera pose, so a longer edge length leads to more strict coverage constraints.

*2) Geometric Viewpoint Generation:* Geometric viewpoint generation produces views $VP_{all}$ from mesh faces of the inspected structure. VGD $d_{VGD}$ modulates viewpoint to mesh face distance during viewpoint generation. A watertight mesh $M$ consists of $N_{face}$ triangle faces $a_i$ with unit-length face normal $\hat{n}_i$, centroid $o_i$, and three corner vertices $e_{i0}$, $e_{i1}$, and $e_{i2}$ (Figure 3). All displacements are measured with respect to frame $F$, with origin located at the center of mass of the International Space Station (ISS) model and axes ${}^F\hat{x}_0$ radially outward from the ISS, ${}^F\hat{x}_1$ tangent to ISS orbit, and ${}^F\hat{x}_2$ along the ISS angular momentum vector. Each viewpoint $q_i$ includes a position coordinate $p_i \in \mathbb{R}^3$ and view direction unit vector $\hat{v}_i \in \mathbb{R}^3$ (Eq. 1). Viewpoint $q_i \in \mathbb{R}^6$ is generated from face $a_i$ geometry by extending surface normal $\hat{n}_i$ a distance $d_{VGD}$ from centroid $o_i$ and pointed at $o_i$ (Eq. 1, Figure 3). Viewpoints that collide with the target structure are discarded.

$$q_i = \begin{bmatrix} p_i \\ \hat{v}_i \end{bmatrix}, \quad p_i = o_i + d_{VGD}\hat{n}_i, \quad \hat{v}_i = -\hat{n}_i \tag{1}$$

*3) Viewpoint Filtering:* Overlap between viewpoints in $VP_{all}$ is too great for traversal to be fuel efficient, but downsampling $VP_{all}$ can produce a smaller viewpoint set while maintaining surface coverage. Downsampling uses angle of incidence (AOI), angle between the camera view direction and triangle mesh surface normal, to quantify coverage quality. First, viewpoint coverage $\mathrm{cvg}(q_i, a_j)$ (Eq. 2) and incident angle $AOI(q_i, a_j)$ (Eq. 3) are measured using ray casting. Coverage of $a_j$ by viewpoint $q_i$ is only valid when $AOI(q_i, a_j) < AOI_{max}$ with $AOI_{max} = 70°$. $AOI_{max}$ was conservatively chosen based on coverage constraints in [21].

$$\mathrm{cvg}(q_i, a_j) = \begin{cases} 1 & e_{j0},\, e_{j1},\, \& \; e_{j2} \text{ are visible from } q_i \\ 0 & else \end{cases} \tag{2}$$

$$AOI(q_i, a_j) = \cos^{-1}\left(\frac{\langle \hat{n}_j, p_i - o_j \rangle}{||p_i - o_j||_2}\right) \tag{3}$$

$$AOI^*(a_j, VP) = \begin{cases} \min(AOI(q_i, a_j) : q_i) & \mathrm{cvg}(q_i, a_j) \\ \pi & otherwise \end{cases} \tag{4}$$

**IEEE Robotics and Automation Letters (RA-L) paper, presented at ICRA 2026, Vienna, Austria. Cite as RA-L paper.**

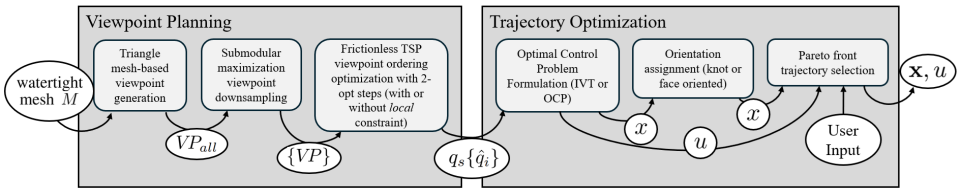


Fig. 1. Stateflow diagram of our approach. $VP_{all}$: all generated viewpoints. $\{VP\}$: minimum set of coverage viewpoints. $q_s, \{q_i\}$: initial state and ordered minimum set of coverage viewpoints. $x$: optimized trajectory state vector. $\mathbf{x}$: Pareto front optimized trajectory state vector. $u$: optimized control actuations.

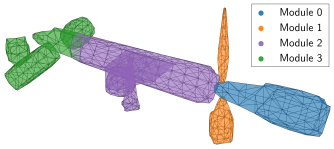


Fig. 2. Station mesh for inspection with color coded module differentiation scaled in diameter to the Destiny module in the ISS (4.2 meters)

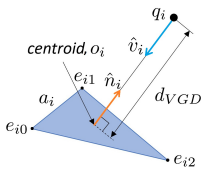


Fig. 3. Viewpoint $q_i$ extended from face $a_i$ centroid $o_i$ along surface normal $\hat{n}_i$ by $d_{VGD}$ with orientation $\hat{v}_i$. Triangle vertices are $e_{i0}$, $e_{i1}$, and $e_{i2}$

The downsampled viewpoint set $VP$ was built by iteratively adding the view that maximizes information gain $\max(IG(q_i, VP) : q_i \in \{VP_{all} \setminus VP\})$ to $VP$ (Eqs. 5 and 6). Viewpoints in the coverage set that fail to increase information gain (i.e. $IG(q_i, \{VP \setminus q_i\}) = 0$) are pruned.

$$dAOI(q_i, a_j, VP) = \max(0, AOI^* - AOI) \tag{5}$$

$$IG(q_i, VP) = \sum_{a_j \in M} \texttt{cvg}(q_i, a_j) dAOI(q_i, a_j, VP) \tag{6}$$

The algorithm terminates when coverage cannot be increased with viewpoint addition (i.e. $\exists q_i \in \{VP\} | \texttt{cvg}(q_i, a_j) \forall a_j \in M$) with size $N_{VP}$.

The *local* constraint applies information gain maximization and coverage termination criteria to each module individually.

### B. Frictionless TSP

A minimum cost ordering of coverage viewpoints found with TSP methodology provides scaffolding for optimizers to generate inspection trajectories. TSP formulations for large sets do not account for orbital dynamics during cost evaluation [32] or only consider static or time-dependent start and end states to compute costs [15], [16]. Viewpoint-to-viewpoint trajectory sequences in space depend on initial velocity, directly influenced by any prior trajectory. The new frictionless TSP integrates prior path traversal to find minimal fuel cost viewpoint traversal sequences by conditioning viewpoint-to-viewpoint path cost on the previously traversed viewpoint.

The frictionless TSP is asymmetric so it requires a cost volume of size $C \in \mathbb{R}^{N_{VP} \times N_{VP} \times N_{VP}}$, where viewpoint-to-viewpoint cost is assigned for every unique sequence of three different viewpoints. The cost $[C]_{ijk}$ of traversing viewpoint $q_j$ to $q_k$ depends on prior viewpoint $q_i$.

We assume a user-defined start point $q_s$, motivated by the use of an ISS docking bay for any refueling or maintenance a free-flying space robotic inspector may require.

*1) Cost Matrix Construction:* Cost matrix construction adds $q_s$ to $\{VP\}$ and computes viewpoint to viewpoint costs given valid prior viewpoints using RRTZ [33]. For each pair of viewpoints $q_j$ and $q_k$ $(i \neq j)$, RRTZ searches for a minimal cost collision free traversal path and stores each trajectory $x_{jk} \in \mathbb{R}^{N_{VP} \times 3}$, where reversing $x_{jk}$ yields $x_{kj}$. At this stage, computing fuel optimal trajectories for every combination of viewpoints is computationally cost prohibitive, so we assume the robot is capable of six degree of freedom instantaneous impulsive maneuvering and is governed by the linearized three body problem summarized by the Clohessy Wiltshire equations. We evaluate cost by discretizing $x_{jk}$ into a series of poses then computing orbital drift opposition fuel costs according to [34]. Transitioning from $x_{ij}$ to $x_{jk}$ requires fuel consumption $c_{ijk}$ to align robot movement with the initial velocity of the second path, so the cost of path $x_{jk}$ conditioned on previously visiting viewpoint $q_i$ is $[C]_{ijk}$ (Eq. 7).

$$[C]_{ijk} = c_{jk} + c_{ijk} \tag{7}$$

Location of this trajectory within the final path is unknown so we assume final mass $m_f = 5[kg]$ is the total inspector robot dry mass based on Mini AERCam [35] when computing fuel consumption $m_{fuel}$ via the Tsiolkovsky rocket equation [36]):

$$m_0 = m_f e^{\Delta v/(I_{sp} g_0)}, \; m_{fuel} = m_0 - m_f \tag{8}$$

Traversal cost of ordered viewpoint set $VP^* = q_0, \ldots, q_{N_{VP}-1}$ is a summation (Eq. 9).

$$\texttt{cost}(VP^*) = c_{0,1} + \sum_{i=0}^{N_{VP}-3} [C]_{i(i+1)(i+2)} \tag{9}$$

*2) Ordering:* The frictionless TSP solver extends the 2-opt algorithm [37], which uses edge swapping to iteratively improve solutions. A new *local* constraint requires all viewpoints corresponding to a specific surface area to be contiguous. The

**IEEE Robotics and Automation Letters (RA-L) paper, presented at ICRA 2026, Vienna, Austria. Cite as RA-L paper.**

2-opt algorithm does not enforce the *local* constraint, so we reject constraint violating improvement steps.

The frictionless TSP solver greedily initializes $VP^*$, improves ordering with the 2-opt method, and satisfies the new *local* constraint. Starting with $q_s$, viewpoints from $VP$ that minimally increase overall traversal cost are sequentially added. A 2-opt move is attempted in each iteration. If path cost (Eq. 9) decreases and *local* constraint is active and satisfied, the 2-opt move is kept; otherwise it is reversed. The final ordered set of knot points $\{\hat{q}_i\}$ of size $N_{knot}$ maximizes coverage and avoids obstacles.

### C. Optimal Control Problem

Optimal control problem formulation in IPopt [38] generates a fuel efficient dynamically feasible path that passes near $\{\hat{q}_i\}$. Solutions are compared directly against an impulsive viewpoint traversal (IVT) strategy. Both approaches assume initial position $q_s$, zero initial velocity, and knot points $\{\hat{q}_i\}$. However, the OCP assumes an actuation at every time step while the IVT assumes actuation only at knot points, leading to similar obstacle avoidance and fuel consumption functions but different trajectory optimization formulations.

*1) Dynamics:* OCP dynamics are governed by the Clohessy Wiltshire equations [39] ($A_{CW}$ in Eq.10) and enforce feasibility for state vector $x \in \mathbb{R}^{N_t \times 6}$, discretized $N_t$ times. Fourth-order Runge-Kutta integration constrains consecutive states according to control input vector $u \in \mathbb{R}^{N_t-1 \times 3}$.

$$\dot{x}_i(x_i, u_i) = A_{CW} x_i + \begin{bmatrix} 0_{3,3} \\ I_3 \end{bmatrix} u_i / m_I \tag{10}$$

where $x_i \in \mathbb{R}^6$ is the $i^{th}$ element of $x$, $u_i \in \mathbb{R}^3$ is the $i^{th}$ element of $u$, $t_i$ is the time step between states $x_i$ and $x_{i+1}$, $\eta = 1.177e-3$ is the orbital rate of the target body (ISS), and $m_I = 5[kg]$ is the simulated robot mass. $N_t = 400$ was chosen for computational feasibility. Time step duration $t_i$ enables constant speed $0.1$ m/s of the straight line path trajectory from ordered viewpoints yielding inspections less than an hour in duration. The IVT assumes an impulsive maneuver $\Delta\bar{v}_i$ at each viewpoint $\hat{q}_i$ that carries the robot to the next viewpoint in time $\bar{t}_i$. Clohessy Wiltshire solutions [40] yield drift trajectories between every consecutive pair of actuation points. Start point $\hat{q}_i$, end point $\hat{q}_{i+1}$, and drift period $\bar{t}_i$ determine initial drift velocity $v_i(\bar{t}_i)$, drift velocity $v_{i,end}(\bar{t}_i)$, and the drift trajectory itself $\bar{x}_i(t)$ for $t \in (0, \bar{t}_i)$. Since $\hat{q}_i$ are static, $\bar{t}_i$ determines $v_i(\bar{t}_i)$ and $v_{i,end}(\bar{t}_i)$. Methods such as Lambert's problem algorithms [41] produce numerically optimal solutions but lack the algebraic simplicity needed for gradient computation in the IVT problem. We therefore apply the CW equations between actuation points during optimization.

*2) Collision Avoidance:* Collision avoidance is enforced by constraining trajectories outside of a convex watertight mesh of the station. Convexity allows an obstacle representation of overlapping half spaces, each defined by a face of the triangular mesh. If a path point is on the outside of any of the boundary mesh planes, the point is collision free.

Location $x \in \mathbb{R}^3$ is collision free if it lies on the outside of one half plane of a convex obstacle represented by $N_{face}$ face normals $\hat{n}$ and centroids $o_i$ (Eq. 11), where $O$ is the closed set of states $x$ that lie inside the convex hull.

$$\begin{aligned} &Let\ r^{x/p_i} = x - o_i \\ &if\ \exists\ i \in \{1, \ldots, N\}\ s.t.\ \langle r^{x/o_i}, \hat{n}_i \rangle > 0\ then\ x \notin O \end{aligned} \tag{11}$$

The OCP enforces collision avoidance on every state while the IVT method enforces collision avoidance on discretized drift trajectories. Each IVT drift period is discretized into $N_{drift}$ time steps $\{\bar{t}_{i,0} \ldots \bar{t}_{i,N_{drift}-1}\}$, and corresponding points $\bar{x}_i(\bar{t}_{i,j})$ are constrained to the free space ($x \notin O$) where $i = 0 \ldots N_{knot} - 1$ and $j = 0 \ldots N_{drift} - 1$. Final paths are manually checked for collision avoidance.

*3) Objective Function:* The objective function penalizes fuel consumption and knot point proximity. The OCP-minimized fuel cost, knot alignment cost, and the IVT together minimized total actuation $\Delta v$. The OCP computed fuel cost from integrated force inputs from $t = 0 \ldots N_t - 1$ (Eq. 12). $g_0$ is the gravitational constant and $I_{sp}$ is specific impulse of the cold gas thruster used for force inputs modeled from [42].

$$f_1(x, u) = \sum_{i=0}^{N_t-1} \frac{\|u[i]\|^2}{g_0 I_{sp}} \tag{12}$$

Knot cost penalizes trajectory deviation from the ordered knot points. Every knot point $\hat{q}_i$ is assigned a set of contiguous states $x^{\hat{q}_i} \in x$ from the straight line paths between knot points. $x^{\hat{q}_i}$ includes state vector elements from halfway between $\hat{q}_i$ and $q_{i-1}$ to halfway between $\hat{q}_i$ and $\hat{q}_{i+1}$. Knot cost is the sum of the squared distances between each knot point $\hat{q}_i$ and the closest state vector $\hat{x} \in x^{\hat{q}_i}$ (Eqs. 13 and 14).

$$y(i, x) = \begin{cases} 1 & (x - \hat{q}_i)^2 = \min\limits_{\hat{x} \in x^{\hat{q}_i}} (\hat{x} - \hat{q}_i)^2 \\ 0 & otherwise \end{cases} \tag{13}$$

$$f_2(x) = \sum_{i=0}^{N_{knot}-1} \sum_{x \in \hat{x}^{\hat{q}_i}} y(i, \hat{x})(\hat{x} - \hat{q}_i)^2 \tag{14}$$

The total objective function is the sum of fuel cost and knot point cost (Eq. 15). $w$ is a user-defined weighting. $\hat{f}_1$ and $\hat{f}_2$ are normalizing constants that balance $f_1$ and $f_2$ such that the terms are equal in magnitude when $w = 0.5$.

$$f(x, u) = w \frac{f_1(x, u)}{\hat{f}_1} + (1 - w) \frac{f_2(x)}{\hat{f}_2} \tag{15}$$

*4) Optimization:* IPopt in CasADi is used to find the set of control inputs that minimize $f(x, u)$ (Eq. 16) while satisfying constraints and initial conditions.

$$\begin{aligned} \min_{x,u} \quad & f(x, u) \\ \text{s.t.} \quad & \texttt{fmax}(r^{x_i/p_1} \cdot \hat{n}_1, \ldots, r^{x_i/p_N} \cdot \hat{n}_N) > 0, \\ & |u[i]|_2 < 1.0, x_i = RK(x_{i-1}, t_i), x_i \notin O, \\ & i = 0 \ldots N_t - 1 \end{aligned} \tag{16}$$

**IEEE Robotics and Automation Letters (RA-L) paper, presented at ICRA 2026, Vienna, Austria. Cite as RA-L paper.**

IVT finds the optimal set of drift periods $\bar{\mathbf{t}}$ that minimizes impulsive maneuvering cost (Eqs. 17 and 18) subject to actuation, maximum duration, and obstacle avoidance constraints (Eq. 19) where $O$ is the occupied obstacle space.

$$\Delta\bar{v}_i(\bar{t}_i, \bar{t}_{i-1}) = \begin{cases} v_i(\bar{t}_i) & i = 0 \\ -v_{i-1,end}(\bar{t}_{i-1}) & i = N_{knot} \\ v_i(\bar{t}_i) - v_{i-1,end}(\bar{t}_{i-1}) & otherwise \end{cases} \quad (17)$$

$$\bar{f}(\bar{t}_i) = \sum_{i=0}^{N_{knot}-1} \|\Delta\bar{v}_i\|_2 \quad (18)$$

$$\begin{aligned} \min_{\bar{t}} \quad & \bar{f}(\bar{t}) \\ \text{s.t.} \quad & \sum_{i=0}^{N_{knot}-1} \bar{t}_i < \bar{t}_{max} \\ & \bar{t}_i > 0,\ \|\Delta\bar{v}_i\|_2 < \Delta\bar{v}_{max},\ \bar{x}_i(t) \notin O \\ & i = 0 \dots N_{knot} - 1 \end{aligned} \quad (19)$$

### D. Orientation Assignment

After Trajectory Generation, path states are assigned camera orientations using Knot Orientation (KO) and Face Orientation (FO) methods. In both methods, each knot point $q_i$ is linked with the closest state $x_{\hat{q}_i}$ in $x^{\hat{q}_i}$. KO assigns the view direction of $x^{\hat{q}_i}$ to $x_{\hat{q}_i}$. FO points $x_{\hat{q}_i}$ toward $o_j$, the centroid $\hat{q}_i$ was generated from (Section II-A2). In both methods, states not assigned an orientation are assigned orientations by applying spherical linear interpolation between KO or FO states. KO and FO are applied to solutions produced by the OCP optimization framework. IVT trajectories do not deviate from knot points, so KO assignment was used to assign IVT orientations.

### E. Pareto Front Construction

We adapt Pareto front methodology to optimize competing objective function terms. Objective function weighting $w$ is selected through a Pareto front objective trade space study. The trade space study varies $w$ with a sigmoid function $\sigma(w_{in}),\ w_{in} \in \{-10, -9.5, \dots, 10\}$ (Eq. 20).

$$w = \sigma(w_{in}) = \frac{1}{1 + e^{-w_{in}}} \quad (20)$$

Final solutions use weightings from optimized state vectors $\mathbf{x}(w)$ to minimize fuel cost and missed coverage $MC(\mathbf{x}(w))$, the fraction of faces $a_j$ without $\texttt{cvg}(x_i, a_j) \forall x_i \in \mathbf{x}$, where $\texttt{fcvg}(a_j, \mathbf{x})$ is true if face $a_j$ is seen from path $\mathbf{x}$.

$$\texttt{fcvg}(a_j, \mathbf{x}) = \begin{cases} 1 & \exists x_i \in \mathbf{x} \text{ s.t. } \texttt{cvg}(x_i, a_j) \\ 0 & otherwise \end{cases} \quad (21)$$

$$MC(\mathbf{x}) = 1 - \sum_{j=0}^{j<N_{face}} \frac{\texttt{fcvg}(a_j, \mathbf{x})}{N_{face}} \quad (22)$$

The inverse relationship between missed coverage and fuel in the Pareto front indicates a tradeoff between coverage and fuel usage (Figure 4). Pareto front solution diversity allows a supervisor to choose a solution that achieves a specific coverage threshold with minimal fuel consumption. The weighting that minimizes fuel consumption with at least 98% station coverage ($MC(\mathbf{x}(w)) < 0.02$) was selected in this study.

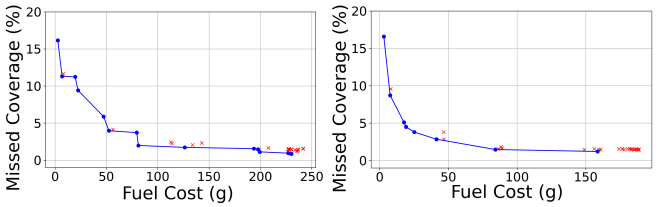


(a) 2m VGD, *local* (b) 2m VGD, *global*

Fig. 4. Each point is a solution with different $w$. Pareto optimal solutions are blue and connected. Suboptimal solutions are red x's

### F. Simulation Parameters

Each trajectory generation method was applied to the station model in Figure 2 for each VGD in $\{2, 4, 8, 16\}$ $[m]$ with and without the *local* constraint. The selection of VGD depends on the desired resolution of the inspection surface. We chose a range that is twice as far as the keepout distance ($2m$) and close enough to resolve 0.5 inch MMOD impacts ($16m$). This range also demonstrates method flexibility to different VGDs and shows its effect on fuel consumption. The IVT generated solutions for each set of ordered knot points for three values of $\bar{t}_{max}$: 10 minutes, 50 minutes, and path duration of the corresponding OCP. Path length in meters and number of knots are measured for all knot point sequences. Fuel cost is computed by integrating the rocket equation [34]. Coverage is the fraction of station faces seen from the inspection trajectory (Eqs. 23 and 25 with helper functions Eqs. 21 and 24).

$$\texttt{cvg}_{OCP}(\mathbf{x}) = \sum_{i=0}^{i<N_{face}} \frac{\texttt{fcvg}(a_i, \mathbf{x})}{N_{face}} \quad (23)$$

$$\texttt{fcvg}_{IVT}(a_j, \bar{\mathbf{t}}) = \begin{cases} 1 & \exists \bar{x}_i(\bar{t}_k),\ i \in \{0 \dots N_{knot} - 1\} \\ & k \in \{0 \dots N_{drift} - 1\} \\ & s.t.\ \texttt{cvg}(a_j, \bar{x}_i(\bar{t}_k)) \\ 0 & otherwise \end{cases} \quad (24)$$

$$\texttt{cvg}_{IVT}(\bar{\mathbf{t}}) = \sum_{i=0}^{i<N_{face}} \texttt{fcvg}_{IVT}(a_j, \bar{\mathbf{t}}) \quad (25)$$

Average slew rate (eigenaxis rotation angle [43]) is measured for the path generated by each method, VGD, and *local* constraint combination. The standardized mean difference measured trajectory optimization method impact on coverage ($SMD = \frac{\mu_{cvg,diff}}{\sigma_{cvg,diff}}$). $\mu_{cvg,diff}$ and $\sigma_{cvg,diff}$ are the mean and standard deviation of paired coverage value differences.

**IEEE Robotics and Automation Letters (RA-L) paper, presented at ICRA 2026, Vienna, Austria. Cite as RA-L paper.**

TABLE I
KNOT POINT SEQUENCES

| VGD | Constraint | $\texttt{cost}(VP^*)$ (g) | Length (m) | $N_{knot}$ |
|---|---|---|---|---|
| 2m | global | 79.93 | 408.22 | 121 |
| 2m | local | 107.11 | 523.63 | 155 |
| 4m | global | 51.05 | 337.98 | 71 |
| 4m | local | 88.94 | 561.48 | 141 |
| 8m | global | 43.14 | 379.16 | 60 |
| 8m | local | 67.96 | 694.13 | 96 |
| 16m | global | 30.65 | 474.26 | 41 |
| 16m | local | 36.76 | 640.31 | 41 |

## III. RESULTS

Knot point sequence (Figure 5, dashed) length and geometry are directly influenced by VGD and locality constraint (Figure I). Knot point sequences with the local constraint are longer in number of knots and length (Table I). Increased VGD leads to more knot points in resulting sequences. Knot point sequence heuristic cost follows a similar pattern to final trajectory fuel cost with respect to VGD and *local* constraint but underestimates long path ($N_{knot} \geq 121$) cost and overestimates short path ($N_{knot} \leq 96$) cost. Final weightings that minimize fuel use for $> 98\%$ coverage are the same positive values for Knot Oriented and Face Oriented view direction assignment methods and increase with VGD. $w = 4.5$ for both 2m $VGD$ conditions, $w = 9$ for both 16m $VGD$ conditions, $w = 7$ for 4m $VGD$ and *global*, $w = 4.5$ for 4m $VGD$ and *local*, $w = 9$ for 8m $VGD$ and *global*, and $w = 7$ for 8m $VGD$ and *local*.

Trajectory generation method, VGD, and *local* constraint impact trends in fuel consumption, coverage percentage, and slew rate. Larger VGDs, no *local* constraint, and OCP optimization (Figure 5, solid) decrease fuel consumption (Table II). IVT trajectories yield higher coverage percentage than Knot Oriented OCP ($SMD = 1.24$, difference $= 0.39\%$) and Face Oriented OCP ($SMD = 1.19$, difference = $0.41\%$) trajectories (Table III). IVT and Face Oriented trajectories have the slowest and second slowest slew rates shown in Tables III and II, respectively. IVT, no *local* constraint and higher VGD lead to the slowest slew rates (Table III).

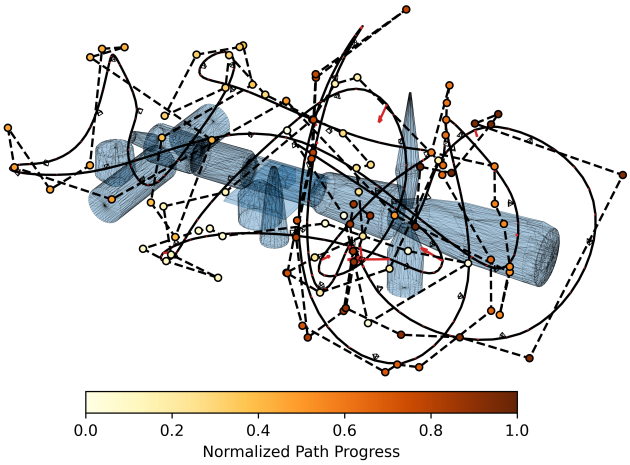


(a) 8m VGD, *local* constraint leads to tighter, more costly turns

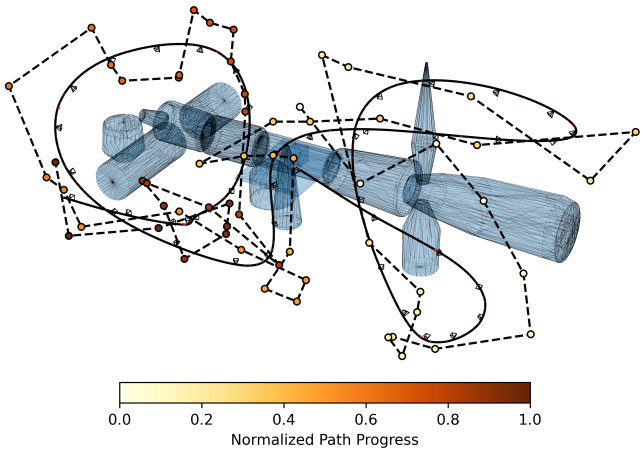


(b) 8m VGD, wider turns in the *global* condition lead to greater fuel efficiency

Fig. 5. OCP solutions (solid), ordered knot points (dashed, colorbar denotes viewpoint order), sparse maneuvers in red

## IV. DISCUSSION AND FUTURE WORK

The presented human supervised robotic inspection system provides an exterior space station inspection alternative that may impose lower risk than astronaut EVA. This paper describes a trajectory generator for in-orbit external space station inspection adapted from terrestrial inspection algorithms. The proposed system can generate trajectories to inspect any in-orbit structure with a 3D watertight mesh. The system generates inspection trajectories by generating coverage viewpoints, ordering viewpoints in a cost minimal way (Figure 5, dashed), then generating a trajectory (Figure 5, solid) that maximizes coverage and minimizes fuel consumption on-orbit. Viewpoint generation distance, trajectory optimization method, orientation assignment method, and *local* constraint that potentially modulates situational awareness are shown to affect fuel consumption and slew rate.

Terrestrial inspection algorithms plus OCP maximize information gain and minimize fuel use. Viewpoint planning [21] and orbital kinodynamics [39] were integrated into viewpoint and trajectory optimization modules. Knot point distance penalties provide the OCP with a direct gradient for information gain optimization. A Pareto front allows a user to balance fuel use with coverage completeness. $w$ values that favor fuel consumption penalty weighting and increase with VGD balance information gain and fuel objectives. Pareto front missed coverage incentives combined with waypoint proximity penalties enable freeform inspection path optimization while current orbital station inspection algorithms constrain paths to spiral patterns [5] or pass through waypoints [8], [9].

VGD and locality modulate fuel consumption when coverage is maximized but may also affect inspection performance. The locality constraint increases fuel consumption but enables situation awareness support modulation analysis to potentially increase a supervisor's ability to detect damage. Increased VGD decreases fuel consumption, but also decreases the quality of the camera view of the surface because the distance between camera and surface is greater. $AOI_{max}$ also modulates camera view quality by determining viewpoint coverage

**IEEE Robotics and Automation Letters (RA-L) paper, presented at ICRA 2026, Vienna, Austria. Cite as RA-L paper.**

TABLE II
TRAJECTORY COMPARISON ACROSS ALL VGD AND *local* CONDITIONS

| | | | Knot Oriented | | | Face Oriented | | | IVT (time matched) | | |
|---|---|---|---|---|---|---|---|---|---|---|---|
| VGD | Constraint | Duration (min) | Fuel (g) | Coverage | Slew (°/s) | Fuel (g) | Coverage | Slew (°/s) | Fuel (g) | Coverage | Slew (°/s) |
| 2m | global | 34.02 | **84.17** | 98.36% | 5.455 | 88.37 | 98.27% | 4.245 | 136.37 | **98.88%** | 3.101 |
| 2m | local | 43.64 | **126.28** | 98.18% | 4.935 | **126.28** | 98.01% | 3.805 | 178.87 | **98.88%** | 2.776 |
| 4m | global | 28.16 | **31.92** | 98.01% | 2.432 | 33.22 | 98.53% | 2.280 | 86.92 | **98.70%** | 1.951 |
| 4m | local | 46.79 | **97.74** | 98.27% | 3.455 | 97.86 | 98.44% | 2.684 | 153.60 | **98.70%** | 1.587 |
| 8m | global | 31.60 | **17.00** | 98.62% | 1.818 | **17.00** | 98.10% | 2.013 | 71.21 | **98.70%** | 1.445 |
| 8m | local | 57.84 | **58.84** | 98.70% | 2.088 | **58.84** | 98.62% | 1.959 | 117.15 | **99.39%** | **1.002** |
| 16m | global | 39.52 | **22.44** | **98.70%** | 0.696 | **22.44** | **98.70%** | 0.777 | 50.06 | **98.70%** | 0.584 |
| 16m | local | 53.36 | **24.28** | **98.70%** | 1.448 | **24.28** | **98.70%** | 0.840 | 60.81 | **98.70%** | **0.606** |

TABLE III
IVT TRAJECTORY COMPARISON ACROSS VGD AND *local* CONDITIONS FOR CONSTANT VALUES OF $\bar{t}_{max}$

| | | IVT, $\bar{t}_{max}$ = 10 min | | | IVT, $\bar{t}_{max}$ = 50 min | | |
|---|---|---|---|---|---|---|---|
| VGD | Constraint | Fuel (g) | Coverage | Slew (°/s) | Fuel (g) | Coverage | Slew (°/s) |
| 2m | global | 477.83 | **98.88%** | 10.559 | 92.69 | **98.88%** | **2.111** |
| 2m | local | 854.43 | **98.88%** | 12.440 | 155.71 | **98.88%** | **2.422** |
| 4m | global | 248.30 | **98.70%** | 5.497 | 48.97 | **98.70%** | **1.103** |
| 4m | local | 769.15 | **98.70%** | 7.647 | 143.63 | **98.70%** | **1.485** |
| 8m | global | 228.28 | **98.70%** | 4.561 | 44.96 | **98.70%** | **0.913** |
| 8m | local | 746.38 | **99.39%** | 6.000 | 135.77 | **99.39%** | 1.159 |
| 16m | global | 198.05 | **98.70%** | 2.297 | 39.78 | **98.70%** | **0.461** |
| 16m | local | 344.24 | **98.70%** | 3.334 | 64.91 | **98.70%** | 0.647 |

thresholds. Investigation into the effect of *local* constraint, VGD, and $AOI_{max}$ threshold on human supervisor damage detection via human study is recommended for future work.

IVT, high VGD, and *local* trajectories modulate factors that may impact human supervisor situation awareness. IVT trajectory generation and no *local* constraint reduce slew rates resulting in slower camera movement. Compared to IVT trajectories, FO assignment trades slow slew rates and coverage for decreased fuel consumption, but improves slew rates compared to KO assignment. Increase in VGD decreases slew rate, but decreases camera to surface distance, which may be detrimental to damage detection. Slower camera movement for an observer may result in less disorientation, potentially impacting supervisor level 1 situation awareness [4]. Using the methodology provided in this paper, future work involving human studies can use these generated trajectories to assess the impact of orientation method, trajectory generation method, VGD, and *local* constraint on supervisor situation awareness and damage detection success in simulated inspection tasks.

Assumptions made in this paper created implementation challenges. Instantaneous impulsive maneuvers assumed in IVT may result in trajectory drift which, if corrected, would lead to increased fuel costs [34]. Without this assumption, viewpoint ordering would require a trajectory cost estimator that may be computationally prohibitive such as optimal control for every tested ordering of viewpoints in the frictionless TSP. Simulations studying the impact of sensor noise and actuation error on information gain and coverage are recommended to inform implementation. Discontinuous gradients caused by the piecewise obstacle avoidance constraint function in local optimization indicate smoother obstacle avoidance functions may improve results. Information gain in viewpoint selection and ordering only accumulates coverage at viewpoints, not during viewpoint to viewpoint traversal. Accounting for coverage between viewpoints is planned future work.

Method limitations yield opportunities for future work. The optimal control problem formulated does not include constraints that consider sun angle, shadows, or camera exposure, but these can be integrated through enforcement during viewpoint generation and orientation assignment phases using attitude constraint optimization from Wang et al. [6]. Simulation methodologies in this paper are limited by the underlying optical and dynamical assumptions. Future work applying this method in simulated space environments or in flight experiments is recommended. Trajectory optimization compute requirements approached the memory limitations of the simulation computer (32 GB of RAM) and negated online optimization capability. Future work into more efficient trajectory optimization that enables online computation is recommended. While trajectories produced are collision-free, the analysis of inspection agent to station distance and its time derivative are recommended to evaluate trajectory safety risk.

## V. CONCLUSION

This paper has presented a trajectory generation pipeline for visual exterior ISS inspection, contributing to a free flying robotic inspection system that reduces astronaut EVA inspection responsibility. The presented method optimizes fuel consumption and coverage for space robot dynamics constrained trajectories leveraging set theory for viewpoint coverage maximization, an extension of TSP methodology for viewpoint ordering, optimal control problem formulation for in-orbit free flyer robot dynamics feasibility, and Pareto front methodology to select balanced fuel and coverage optimized solutions. The OCP trajectory generation method minimizes fuel consumption and leverages a knot point proximity objective function to reward information gain maximization.

**IEEE Robotics and Automation Letters (RA-L) paper, presented at ICRA 2026, Vienna, Austria. Cite as RA-L paper.**

The modular trajectory generation pipeline offers potential situation awareness support modulation at the expense of fuel. Future human studies investigating the impact of these factors on situation awareness support and damage detection for a human supervisor is the subject of ongoing research. The inspection trajectory generation method for orbital proximity operations in this paper is a step towards increasing astronaut safety, while preserving external visual inspection capabilities.

## REFERENCES


[1] R. Moore, "ISS Inspection Capabilities and Challenges," NASA Johnson Space Center, Jul. 2014.

[2] S. Fredrickson, S. Duran, A. Braun, T. Straube, and J. Mitchell, "AERCam Autonomy: Intelligent Software Architecture for Robotic Free Flying Nanosatellite Inspection Vehicles," in *Space*. AIAA, 2006.

[3] S. Pedrotty, J. Sullivan, E. Gambone, and T. Kirven, "Seeker Free-Flying Inspector GNC System Overview," in *AAS GNC Conference*, Feb. 2019.

[4] M. R. Endsley, "Toward a Theory of Situation Awareness in Dynamic Systems," *Human Factors*, vol. 37, no. 1, pp. 32–64, Mar. 1995, publisher: SAGE Publications Inc.

[5] S. Faghihi, S. Tavana, and A. de Ruiter, "Multiple spacecraft coordination and motion planning for full-coverage inspection of large complex space structures," *Acta Astronautica*, vol. 202, pp. 119–129, Jan. 2023.

[6] K. Wang, J. Qiao, E. Wang, J. Lei, W. Wang, and T. Meng, "Safe Inspection Tracking Control for a Tumbling Target Under Full State Constraints and Limited Thrust," *IEEE Transactions on Aerospace and Electronic Systems*, pp. 1–18, 2025.

[7] F. Capolupo and P. Labourdette, "Receding-Horizon Trajectory Planning Algorithm for Passively Safe On-Orbit Inspection Missions," *Journal of Guidance, Control, and Dynamics*, vol. 42, no. 5, pp. 1023–1032, 2019.

[8] N. Ortolano, D. K. Geller, and A. Avery, "Autonomous Optimal Trajectory Planning for Orbital Rendezvous, Satellite Inspection, and Final Approach Based on Convex Optimization," *The Journal of the Astronautical Sciences*, vol. 68, no. 2, pp. 444–479, Jun. 2021.

[9] K. Wang, T. Meng, W. Wang, and J. Lei, "Control barrier function based trajectory generation and tracking control for spacecraft inspection mission under multiple safety constraints," *Advances in Space Research*, vol. 73, no. 3, pp. 2080–2097, Feb. 2024.

[10] Y. K. Nakka, W. Hönig, C. Choi, A. Harvard, A. Rahmani, and S.-J. Chung, "Information-Based Guidance and Control Architecture for Multi-Spacecraft On-Orbit Inspection," *Journal of Guidance, Control, and Dynamics*, vol. 45, no. 7, pp. 1184–1201, Jul. 2022, publisher: American Institute of Aeronautics and Astronautics.

[11] B. Englot and F. S. Hover, "Three-dimensional coverage planning for an underwater inspection robot," *Intl. J.of Robotics Research*, vol. 32, no. 9-10, pp. 1048–1073, Aug. 2013, sAGE Publications.

[12] M. Roberts, D. Dey, A. Truong, S. Sinha, S. Shah, A. Kapoor, P. Hanrahan, and N. Joshi, "Submodular Trajectory Optimization for Aerial 3D Scanning," in *Proceedings of the IEEE International Conference on Computer Vision (ICCV)*, Oct. 2017.

[13] N. Smith, N. Moehrle, M. Goesele, and W. Heidrich, "Aerial path planning for urban scene reconstruction: a continuous optimization method and benchmark," *ACM Trans. Graph.*, vol. 37, no. 6, Dec. 2018.

[14] B. Hepp, M. Nießner, and O. Hilliges, "Plan3D: Viewpoint and Trajectory Optimization for Aerial Multi-View Stereo Reconstruction," *ACM Transactions on Graphics*, vol. 38, no. 1, pp. 4:1–4:17, Dec. 2018.

[15] L. Hou and A. Misra, "Traveling Salesman Problem of optimal debris removal sequence using non-population gradient search," *Acta Astronautica*, vol. 215, pp. 373–386, Feb. 2024.

[16] R. Gupta and S. J. Nanda, "Solving time varying many-objective TSP with dynamic ϑ-NSGA-III algorithm," *Applied Soft Computing*, vol. 118, p. 108493, Mar. 2022.

[17] E. Dunn and G. Olague, "Pareto optimal camera placement for automated visual inspection," in *2005 IEEE/RSJ Intl. Conf. on Intelligent Robots and Systems*, Aug. 2005, pp. 3821–3826, iSSN: 2153-0866.

[18] K. O. Ellefsen, H. A. Lepikson, and J. C. Albiez, "Planning Inspection Paths through Evolutionary Multi-objective Optimization," in *Proc. Genetic and Evolutionary Computation Conference*, ser. GECCO '16. New York, NY, USA: Association for Computing Machinery, Jul. 2016.

[19] T. B. Sheridan, "Supervisory Control," in *Handbook of Human Factors and Ergonomics*. John Wiley & Sons, Ltd, 2006, pp. 1025–1052.

[20] R. Parasuraman, T. Sheridan, and C. Wickens, "A model for types and levels of human interaction with automation," *IEEE Transactions on Systems, Man, and Cybernetics - Part A: Systems and Humans*, vol. 30, no. 3, pp. 286–297, May 2000, conference Name: IEEE Transactions on Systems, Man, and Cybernetics - Part A: Systems and Humans.

[21] P. Gospodnetić, D. Mosbach, M. Rauhut, and H. Hagen, "Viewpoint placement for inspection planning," *Machine Vision and Applications*, vol. 33, no. 1, p. 2, Oct. 2021.

[22] E. Galceran and M. Carreras, "A survey on coverage path planning for robotics," *Rob. & Auto. Sys.*, vol. 61, no. 12, pp. 1258–1276, Dec. 2013.

[23] B. Englot and F. S. Hover, "Sampling-based sweep planning to exploit local planarity in the inspection of complex 3D structures," in *2012 IEEE/RSJ International Conference on Intelligent Robots and Systems*, Oct. 2012, pp. 4456–4463, iSSN: 2153-0866.

[24] C. Cao, J. Zhang, M. Travers, and H. Choset, "Hierarchical Coverage Path Planning in Complex 3D Environments," in *2020 IEEE International Conference on Robotics and Automation (ICRA)*, May 2020, pp. 3206–3212, iSSN: 2577-087X.

[25] J. D. Lee and K. A. See, "Trust in Automation: Designing for Appropriate Reliance," *Human Factors*, vol. 46, no. 1, pp. 50–80, Mar. 2004.

[26] G. Papadopoulos, H. Kurniawati, and N. M. Patrikalakis, "Asymptotically optimal inspection planning using systems with differential constraints," in *2013 IEEE International Conference on Robotics and Automation*, May 2013, pp. 4126–4133, iSSN: 1050-4729.

[27] A. Bircher, K. Alexis, U. Schwesinger, S. Omari, M. Burri, and R. Siegwart, "An incremental sampling-based approach to inspection planning: the rapidly exploring random tree of trees," *Robotica*, vol. 35, no. 6, pp. 1327–1340, Jun. 2017.

[28] G. H. Tarbox and S. N. Gottschlich, "Planning for Complete Sensor Coverage in Inspection," *Computer Vision and Image Understanding*, vol. 61, no. 1, pp. 84–111, Jan. 1995.

[29] W. R. Scott, G. Roth, and J.-F. Rivest, "View planning for automated three-dimensional object reconstruction and inspection," *ACM Comput. Surv.*, vol. 35, no. 1, pp. 64–96, Mar. 2003.

[30] A. Krause and D. Golovin, "Submodular function maximization." *Tractability*, vol. 3, no. 71-104, p. 3, 2014.

[31] T. Ju, F. Losasso, S. Schaefer, and J. Warren, "Dual contouring of hermite data," in *Proc. of the 29th Conference on Computer Graphics and Interactive Techniques*, ser. SIGGRAPH '02. New York, NY, USA: Association for Computing Machinery, Jul. 2002, pp. 339–346.

[32] R. Tinós, K. Helsgaun, and D. Whitley, "Efficient Recombination in the Lin-Kernighan-Helsgaun Traveling Salesman Heuristic," in *Parallel Problem Solving from Nature – PPSN XV*, A. Auger, C. M. Fonseca, N. Lourenço, P. Machado, L. Paquete, and D. Whitley, Eds. Cham: Springer International Publishing, 2018, pp. 95–107.

[33] B. Apodaca, E. Atkins, and L. Stirling, "RRTZ: a Path Planner Designed for Zero Gravity," in *2024 IEEE Aerospace Conf.*, Mar. 2024.

[34] B. Apodaca, L. Stirling, and E. Atkins, "Orbital dynamic effects on fuel use in sampling-based plans for proximity operations," *Journal of Spacecraft and Rockets*, Mar. 2025, published online.

[35] S. E. Fredrickson, "Mini AERCam for In-Space Inspection," Houston, TX, Feb. 2012, nTRS Author Affiliations: NASA Johnson Space Center NTRS Report/Patent Number: JSC-CN-25800 NTRS Document ID: 20120002583 NTRS Research Center: Johnson Space Center (JSC).

[36] K. E. Tsiolkovsky, *The Exploration of Outer Space by Means of Rocket Devices*. University of California Press, 1952.

[37] G. A. Croes, "A Method for Solving Traveling-Salesman Problems," *Operations Research*, vol. 6, no. 6, pp. 791–812, 1958, INFORMS.

[38] A. Wächter and L. T. Biegler, "On the implementation of an interior-point filter line-search algorithm for large-scale nonlinear programming," *Mathematical Programming*, vol. 106, no. 1, pp. 25–57, Mar. 2006.

[39] W. H. Clohessy and R. S. Wiltshire, "Terminal Guidance System for Satellite Rendezvous," *Journal of the Aerospace Sciences*, vol. 27, no. 9, pp. 653–658, Sep. 1960, Amer. Inst. of Aeronautics and Astronautics.

[40] H. D. Curtis, "Chapter 7 - Relative Motion and Rendezvous," in *Orbital Mechanics for Engineering Students (Third Edition)*, H. D. Curtis, Ed. Boston: Butterworth-Heinemann, Jan. 2014, pp. 367–404.

[41] R. Battin, *An Introduction to the Mathematics and Methods of Astrodynamics*. Amer. Inst. of Aeronautics and Astronautics, 1987.

[42] C. Bridges, B. Taylor, N. Horri, C. Underwood, S. Kenyon, J. Barrera-Ars, L. Pryce, and R. Bird, "STRaND-2: Visual inspection, proximity operations & nanosatellite docking," in *2013 IEEE Aerospace Conference*, Mar. 2013, pp. 1–8.

[43] B. Wie, *Space Vehicle Dynamics and Control*, ser. AIAA education series. American Institute of Aeronautics and Astronautics, 1998.